

Multidimensional Disorder in Zeolite IM-18 Revealed by Combining Transmission Electron Microscopy and X-ray Powder Diffraction Analyses

Magdalena O. Cichocka,[†] Yannick Lorgouilloux,^{‡,§} Stef Smeets,[†] Jie Su,[†] Wei Wan,[†] Philippe Caullet,[‡] Nicolas Bats,[§] Lynne B. McCusker,^{†,||} Jean-Louis Paillaud,^{*,‡,⊥} and Xiaodong Zou^{*,†}

[†]Berzelii Center EXSELENT on Porous Materials and Inorganic and Structural Chemistry, Department of Materials and Environmental Chemistry, Stockholm University, Stockholm SE-106 91, Sweden

[‡]Université de Haute-Alsace, CNRS, IS2M UMR 7361, F-68100 Mulhouse, France

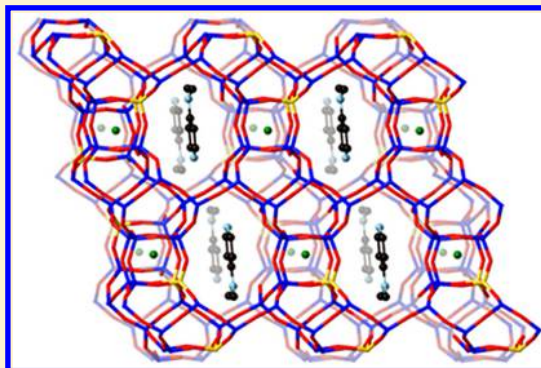
[§]IFP Energies nouvelles, Rond-point de l'échangeur de Solaize - BP 3, 69360 Solaize, France

^{||}Department of Materials, ETH Zurich, CH-8093 Zurich, Switzerland

[⊥]Université de Strasbourg, France

S Supporting Information

ABSTRACT: A new medium-pore germanosilicate, denoted IM-18, with a three-dimensional $8 \times 8 \times 10$ -ring channel system, has been prepared hydrothermally using 4-dimethylaminopyridine as an organic structure-directing agent (OSDA). Due to the presence of stacking disorder, the structure elucidation of IM-18 was challenging, and a combination of different techniques, including electron diffraction, high-resolution transmission electron microscopy (HRTEM), and Rietveld refinement using synchrotron powder diffraction data, was necessary to elucidate the details of the structure and to understand the nature of the disorder. Rotation electron diffraction data were used to determine the average structure of IM-18, HRTEM images to characterize the stacking disorder, and Rietveld refinement to locate the Ge in the framework and the OSDA occluded in the channels.



INTRODUCTION

Since the discovery of the first microporous pure germanates ASU-7¹ (ASV-type framework²) and FOS-S³ (BEC), the search for zeolites with original topologies in the (Si, Ge) system has been prolific.^{4,5} Compared to silicate zeolites, the longer Ge–O bond distance (1.71 Å) and the more flexible O–Ge–O angles favor the formation of double 4-rings (*d4r*)^{6,7} and allow framework topologies that are difficult or even unfeasible in the aluminosilicate system to be synthesized.^{8–14} As a rule, after the discovery of a new zeolitic material, the structure is determined from single-crystal X-ray diffraction (SXRD), high-resolution powder X-ray diffraction (PXRD), or, in recent years, single-crystal electron diffraction data.¹⁵ Depending on the material and its structural complexity, the procedure can be anywhere from routine to highly complex. If, for example, the data are of unavoidably poor quality, the material contains elements of structural disorder, the crystals are radiation sensitive or otherwise difficult to handle, or the crystal structure is simply complex, structure elucidation will be difficult. For those materials that resist structure determination using conventional methods, a combination of techniques is usually required.^{12,16–24}

Materials with structural disorder, such as stacking faults, are particularly notorious for being difficult to characterize structurally and often require creative and nonconventional approaches. For example, in the case of zeolite beta, electron diffraction (ED) patterns and high-resolution transmission electron microscopy (HRTEM) images were used to find the space group and unit cell parameters and to construct possible models. These models were then validated by simulating the corresponding PXRD patterns.^{17,18} The program DIFFaX,²⁵ which is now regularly used to simulate PXRD patterns of structural models containing stacking faults, was initially developed to characterize zeolite beta. A very similar approach was used to determine the disordered structure of the zeolite ITQ-39,²³ which has a three-dimensional (3D) 12- and 10-ring pore system. Two-dimensional (2D) slices from rotation electron diffraction (RED)²⁶ data and HRTEM images indicated the presence of 2D disorder.²³ The structure of ITQ-39 was eventually obtained from the 3D electrostatic potential map from HRTEM images along different directions

Received: January 14, 2018

Revised: February 21, 2018

Published: February 27, 2018

and then confirmed by using the program DIFFaX.²⁵ The structure analysis of SSZ-52 is another example in which PXRD, HRTEM, simulations, and molecular modeling techniques were combined to characterize stacking disorder.²⁴ The framework structure of the zeolite ZSM-48¹⁹ is also highly disordered, and simulations of the faulted structure showed that nine polytypes were possible.

Three-dimensional disorder has been observed in mordenite,²⁰ where the SXRD data showed diffuse scattering, which was modeled using the program DIFFUSE.²⁷ Another example is SSZ-57, whose SXRD pattern shows both diffuse scattering and satellite reflections.²¹ An 8-fold modulation resulting from the presence of a 12-ring in what is otherwise a row of 10-rings gives rise to the satellite reflections. Different models of the local structure were optimized using an evolutionary algorithm and used to simulate the diffuse scattering resulting from the placement of this 12-ring and thereby elucidate the real structure. In an independent study a year earlier, HRTEM images of SSZ-57 were recorded, but a full interpretation of the framework structure was not possible from these images alone.²²

All the techniques described above provide information that can be critical to a successful structure determination, especially if the structure is disordered. If streaking is observed in ED data, the structure will be disordered and the positions and directions of the streaks contain useful information regarding the nature of that disorder. It may be possible to obtain an initial model of the structure, despite this streaking, but other techniques such as HRTEM are required to discern the nature of the disorder. However, not all details can be derived from HRTEM images alone. The location of the heteroatoms in the framework, the fluoride ions, the organic structure directing agents (OSDAs) in the channels, and the refinement of atomic positions still require X-ray diffraction data. Only through a combination of several of these techniques can a detailed elucidation of the structure be achieved.

Here, we describe our efforts to characterize and understand the intriguing crystal structure of IM-18, a germanosilicate zeolite that was discovered more than 10 years ago.²⁸ It was synthesized with 4-dimethylaminopyridine (DMAP) as the OSDA (Figure 1). In fluoride medium, DMAP is efficient for

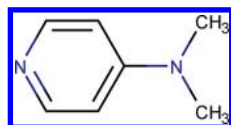


Figure 1. 4-Dimethylaminopyridine (DMAP).

the synthesis of SSZ-51, an aluminophosphate with the SFO²⁹ framework type with a two-dimensional (2D) pore system consisting of intersecting 12- and 8-ring channels. The structure determination of as-made SSZ-51 revealed a π -stacking of the DMAP molecules along the 12-ring channels, suggesting that DMAP played an important role in the formation of the channel. Therefore, we applied DMAP as the OSDA in a (Si,Ge)-system in an attempt to synthesize an SFO-type zeolite or a new topology containing 12-ring channels and $d4r$ units. The crystals that were formed proved to have many of the characteristics that preclude straightforward structure determination, so we performed the structure determination using a combination of RED, HRTEM, and synchrotron PXRD data.

EXPERIMENTAL SECTION

Synthesis of IM-18. Hydrothermal syntheses were performed at 170 °C for 14 days in a homemade multiautoclave containing eight 2 mL Teflon-lined reactors. Gels were prepared in fluoride media by mixing TEOS (>98%, Fluka), amorphous germanium oxide GeO₂ (>99.99%, Aldrich), hydrofluoric acid (HF 40%, Carlo Erba), deionized water, and DMAP (>98%, Fluka). The final products were recovered by filtration, washed several times with deionized water, and then dried at 70 °C for 24 h. The most representative syntheses are reported in Table 1. The corresponding laboratory PXRD data are shown in Figure S2.

Table 1. Selection of the Most Representative Hydrothermal Syntheses Performed under Static Conditions at 170 °C for 14 Days in the (Si, Ge) System with DMAP as the OSDA^a

sample	molar synthesis mixture compositions				products ^{c,d}
	Si/Ge	DMAP/T ^b	HF/T ^b	H ₂ O/T ^b	
1	0.4:0.6	0.5	0.5	8	Q + A
2	0.6:0.4	0.5	0.5	8	Q + A + IM-18
3	0.75:0.25	0.5	0.5	8	IM-18 + A + Q
4	0.8:0.2	0.5	0.5	8	IM-18
5	0.9:0.1	0.5	0.5	8	ZSM-48 + A
6	0.95:0.05	0.5	0.5	8	ZSM-48 + A
7	1:0	0.5	0.5	8	ZSM-48
8	0.6:0.4	0.25	0.5	8	Q + A
9	0.6:0.4	0.75	0.5	8	IM-18 + A + Q
10	0.6:0.4	1	0.5	8	IM-18 + A
11	0.6:0.4	1	1	8	A + IM-18
12	0.8:0.2	1	1	8	IM-18 + NON + C + A
13	0.8:0.2	0.25	0.25	8	ZSM-48 + A
14	0.6:0.4	1	1	20	A + Q + IM-18
15	0.8:0.2	1	1	20	IM-18 + C
16	0.8:0.2	0.5	0.5	3	IM-18 + ϵ NON
17	0.8:0.2	0.5	0.25	3	IM-18 + ϵ C
18	0.8:0.2	0.75	0.5	3	IM-18
19 ^e	0.8:0.2	0.5	0.5	8	IM-18 + A
20 ^f	0.8:0.2	0.5	0.5	8	IM-18 + A + ϵ NON

^aSilica source is TEOS. ^bT = Si + Ge. ^cAs determined from laboratory PXRD (Figure S1). ^dQ = quartz; A = argutite, a dense GeO₂ phase; C = cristobalite, a dense SiO₂ phase; NON = NON-type zeolite. ^e30 days. ^fWith stirring.

Characterization. ¹⁹F magic angle spinning (MAS) NMR experiments were performed on a Bruker Avance II 400 MHz spectrometer (frequency 376.52 MHz, pulse width 4.5 μ s, flip angle $\pi/2$, recycling time 107 s, spinning rate 20 kHz, number of scans 54, and chemical shift standard CFCl₃).

The laboratory PXRD data were collected between 5 and 50° 2 θ (step 0.01°) in Debye–Scherrer geometry on a STOE STADI-P diffractometer equipped with a linear position-sensitive detector (6° in 2 θ) and employing Ge-monochromated CuK α radiation ($\lambda = 1.5406$ Å). The changes in the PXRD patterns with temperature were followed on a PANanalytical X'Pert PRO MPD diffractometer (Cu-K α radiation) equipped with an X'Celerator real-time multiple strip detector and an Anton Paar HTK1200 heating chamber in flat plate reflection geometry (sample cup made of Al₂O₃).

For the 3D rotation electron diffraction (RED) data, a total of 649 ED frames were collected with a step size of 0.20° and an exposure time of 1 s per frame, covering a tilt range of –66.83° to 53.63° (Table S1). Data were collected using the software RED-data collection²⁶ on a JEOL JEM2100 transmission electron microscope (TEM) operating at 200 kV. The RED-data processing software²⁶ was used to reconstruct the 3D reciprocal lattice of IM-18 (Figure S3, Movie in Supporting

Information), to determine the unit cell, and to extract the reflection intensities.

The TEM sample of as-made IM-18 was prepared by crushing the powder, dispersing it in ethanol, and putting a droplet of the suspension on a carbon-coated grid (see Supporting Information). The energy dispersive spectroscopy (EDS) measurements (Table S2) were performed with a JEOL detector on a JEOL JEM 2100F transmission electron microscope. The specimens were tilted 15° with respect to the detector to orient them in an optimal position for the analysis. A through-focus series of 12 HRTEM images with a defocus step of 85.3 Å was taken along the *b*-axis of IM-18 on a JEOL JEM2100F TEM operating at 200 kV. The structure projection was reconstructed using QFocus.³⁰

For the Rietveld analysis,³¹ high-resolution PXRD data were collected on the beamline CRISTAL at the Synchrotron Soleil (France).^{32,33} A monochromatic beam with a wavelength of 0.7294 Å was selected from the undulator beam using a double crystal Si(111) monochromator. Calibration of the wavelength was performed by measuring the diffraction pattern of the Standard Reference Material LaB₆ (SRM660a). Samples of as-made IM-18 were prepared in a 1 mm diameter glass capillary, which was mounted on a two circle diffractometer equipped with a bank of 13 Si(111) analyzer crystals. With this setup, it took approximately 2 h in continuous scanning mode to collect the diffraction pattern. The final data set used for refinement was obtained from the precise superposition and addition of data from the 13 channels.

Thermogravimetric (TGA) and differential thermal analyses (DTA) were performed in air on a Setaram Labsys thermoanalyzer with a heating rate of 5 °C/min up to 1000 °C.

The microporous volume was determined from nitrogen adsorption isotherms obtained at 77 K on a Micromeritics ASAP 2010 porosimeter using the t-plot method.³⁴ After calcination (550 °C in air) the sample was placed in a glass measurement cell and was then degassed at 350 °C under vacuum prior to the measurement.

RESULTS

Synthesis Parameters. It is known that the use of DMAP as the OSDA in hydroxide medium results in a mixture of ZSM-48-type material (topology *MRE)^{19,35} and quartz. However, in fluoride medium, a new phase, denoted IM-18, was obtained. In this section we discuss several parameters that were taken into account in order to optimize the synthesis of IM-18. In all the syntheses summarized in Table 1, the initial and final pH values are identical (pH_i ≈ 8.5 and pH_f ≈ 9).

Variation of the Si/Ge Molar Ratio. When the germanium content is higher than in the synthesis of sample 2, only dense phases are obtained (sample 1), while an increase in the Si/Ge ratio favors the formation of IM-18. However, this observation is valid only up to a certain limit. When the Si/Ge ratio in the mixture is greater than 4, IM-18 no longer crystallizes, and the product harvested contains an *MRE-type material. IM-18 is thus obtained under these conditions only when the Si/Ge ratio is between 1.5 and 4.0.

Modification of the Amount of DMAP and HF. When the synthesis mixture contains more HF than DMAP, the IM-18 phase does not crystallize (sample 8). When the DMAP content is increased, a slight improvement is observed, and the proportion of dense phases decreases (samples 9 and 10). These changes are probably correlated with the pH values, the initial pH values being 7, 7.5, 9.5, and 10.5 for samples 8, 2, 9, and 10, respectively. A joint increase in the amounts of HF and DMAP seems rather detrimental to the synthesis of IM-18 (sample 11). For higher silicon contents, an increase in the DMAP and HF contents lead to the formation of a NON-type phase in addition to that of IM-18 and dense phases (sample

12, pH_i 9.5), while a reduction leads to the production of ZSM-48 and no IM-18 (sample 13, pH_i 7.5).

Modification of the Amount of Water, HF, and DMAP. With a Si/Ge ratio of 1.5, the formation of silicogermanate IM-18 is accompanied by the formation of the same dense phases that appear when the synthesis medium is more dilute (sample 14). However, with a Si/Ge ratio of 4, better results are obtained. Synthesis 4 yields pure IM-18. The purpose of the syntheses of 15–18 was to form crystals of larger size and possibly fewer defects in order to obtain a better X-ray diffraction pattern. In diluted medium, cristobalite cocrystallizes with IM-18 (sample 15). In concentrated media, samples 15 and 16 contain a small amount of impurity, but sample 17 contains pure IM-18.

Finally, we also modified two physical parameters, namely, the synthesis duration and the agitation of the system. While IM-18 appears to be pure in sample 4, an increase in the duration of the synthesis results in the cocrystallization of argutite (sample 19). With stirring, additional cristobalite and a small amount of nonasil result (sample 20).

The germanosilicate PKU-16 (POS) was synthesized using the same OSDA (DMAP) from a gel of composition 0.5GeO₂/0.5SiO₂/5H₂O/0.5DMAP/0.5HF at 125 °C,³⁶ a temperature that is lower than what is required for IM-18 (170 °C).

Because of its purity, sample 4 was used for all characterization experiments, including the structure elucidation.

Scanning Electron Microscopy. The SEM image of IM-18 (sample 4, Figure 2) shows small and irregular thin plates,

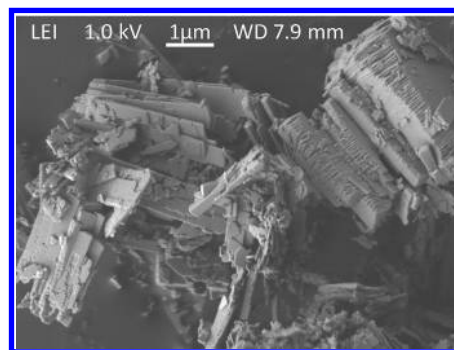


Figure 2. SEM micrograph of IM-18 (sample 4).

which are seen in the TEM images (Figure S1). These platelets have dimensions of the order of $1.5 \times 1.5 \times 0.05 \mu\text{m}^3$. The smaller crystals tend to be more ordered than the larger ones; the latter tend to be intergrown.

¹⁹F Solid State NMR. The ¹⁹F MAS NMR spectrum of IM-18 (sample 4) contains two resonances with chemical shifts of −9.8 and −20.6 ppm, whose relative intensities are 92 and 8%, respectively (Figure 3). These positions probably correspond to fluoride ions occluded within *d4r* units with different germanium content. The values are similar to those determined for the silicogermanate ITQ-7 (ISV, $\delta = -8$ and -20 ppm).³⁷ Blasco et al. assigned the resonance at −20 ppm to a fluoride ion at the center of a *d4r* unit with seven silicon and one germanium and the resonance at −8 ppm to one with five (or four) Si and three (or four) Ge (Figure 3).^{37–39}

Structure Determination of IM-18. Average Structure and Indication of Disorder from Electron Diffraction Data. The RED data collected on an as-made sample of IM-18 (sample 4) could be indexed with a body-centered orthorhombic unit cell, with lattice parameters $a = 5.31 \text{ \AA}$, b

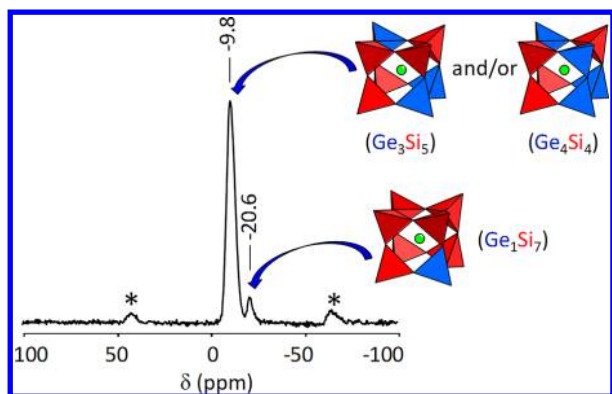


Figure 3. ^{19}F MAS NMR of as-made IM-18 (sample 4) and the corresponding representations of the possible composition of the $d4r$ units. * indicates spinning bands.

$= 15.07 \text{ \AA}$, $c = 17.06 \text{ \AA}$, $\alpha = 89.79^\circ$, $\beta = 88.81^\circ$, and $\gamma = 90.35^\circ$. From the 2D slices (Figure S3) cut from the 3D reciprocal lattice reconstructed from the RED data, we could deduce the reflection conditions to be hkl : $h + k + l = 2n$ and $hk0$: $h = 2n$, $k = 2n$, which are consistent with the space groups $Im2a$ (No. 46) or $Imma$ (No. 74). Considering that most zeolite frameworks in the Database of Zeolite Structures² are centrosymmetric, we first attempted to determine the structure in the space group $Imma$. Although some diffuse scattering was observed in the RED data along the b^* - and c^* -axes, only the intensities of the Bragg diffraction spots were used. Direct methods, as implemented in SHELXS,⁴⁰ revealed an average framework structure that was highly disordered. We were able to distinguish three unique T-atoms ($T = \text{Si}/\text{Ge}$) in the asymmetric unit, which formed two superimposed tetrahedral networks, related by a translation of 5.31 \AA along the a -axis. To disentangle the disorder, we constructed a new model by doubling the unit cell along the a -axis ($Imma$, $a = 2 \times 5.31 \text{ \AA}$, $b = 15.07 \text{ \AA}$, $c = 17.06 \text{ \AA}$), and removing one of frameworks. Missing O atoms were added between the Si atoms, and the structure was optimized by distance least-squares refinement using the program DLS-76.⁴¹ This framework model can be described as a set of zigzag chains along the a -axis interconnected via $d4r$ units to create a 3D channel system with two types of 8-ring channels running parallel to the a -axis, 8-ring channels parallel to the c -axis, and 10-ring channels parallel to the b -axis (Figure S4). The presence of the $d4r$ s is

corroborated by the ^{19}F MAS NMR spectrum, which shows signals characteristic of fluoride ions in a $d4r$ unit (see above, and Figure 3).

Disorder from Selected Area Electron Diffraction (SAED) Patterns. To get a better idea of the nature of the disorder, we first collected selected area electron diffraction (SAED) data (Figure 4), which show diffuse scattering in the low-order zone-axis patterns more clearly than do the RED data. SAED patterns along $[010]$ (Figure 4B) show that all reflections with $h = 2n$ are sharp, while reflections with $h = 2n + 1$ only appear as streaks along c^* . This indicates that there is stacking disorder in the crystal, specifically that the stacking direction is parallel to c^* , and that layers can be translated by $\pm 1/2a$. These patterns also indicate a possible twin plane perpendicular to the c^* -axis. Due to preferred orientation of the plate-like crystals, we were unable to obtain SAED patterns along the c -axis. However, the $hk0$ plane cut from the RED data shows that there are also diffuse streaks for reflections with $h = 2n + 1$ along the b^* -axis (Figure 4C), indicating that there is also stacking disorder parallel to b^* with a translation of $\pm 1/2a$ between the layers perpendicular to b^* . For comparison, the SAED pattern along $[100]$ is free of streaks (Figure 4A), indicating that there is no disorder in the projection along the a -axis in this particular crystal. However, we have observed some weak diffuse scattering in a few crystals in the SAED patterns along $[100]$ (Figures S8 and S9).

Disorder from High-Resolution Transmission Electron Microscopy (HRTEM) Images. HRTEM images were used to describe the local structure and stacking faults in IM-18. It was challenging to take HRTEM images of this particular zeolite because, like most germanosilicates, it is highly sensitive to the beam and easily damaged. To alleviate this problem, we used the through-focus method⁴² for structure projection reconstruction from a series of HRTEM images acquired with a constant-step change in defocus. Because the acquisition and focusing time are minimized, it is ideal for studying beam-sensitive materials. The optimal focus is determined in a subsequent processing step, and the signal-to-noise ratio is greatly enhanced. The contrast of the reconstructed HRTEM image is thus improved, and the image can be interpreted directly in terms of the structure projection. Several through-focus series of 12 HRTEM images with a defocus step of 85.3 \AA were taken manually along the b -axis of IM-18, and the projections were reconstructed using the program QFocus.³⁰

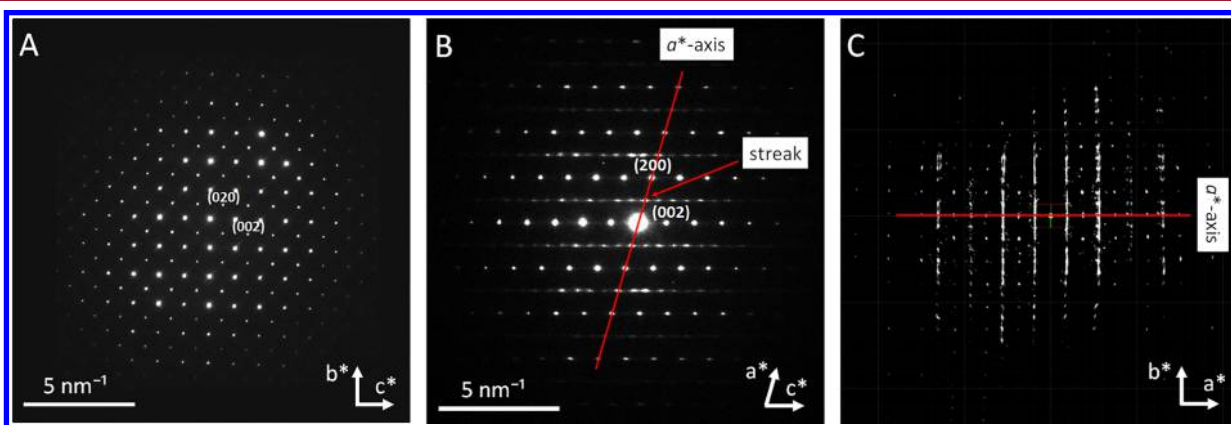


Figure 4. Selected area electron diffraction patterns along (A) $[100]$ and (B) $[010]$ and (C) 2D $hk0$ slice cut from the reconstructed 3D reciprocal lattice showing the diffuse scattering.

Structure projections along the b -axis confirmed that our structural model was reasonable but also revealed the presence of both ordered and disordered regions. The disordered region can also be recognized by the streaks in the corresponding Fourier transform that is inset in Figure 5A.

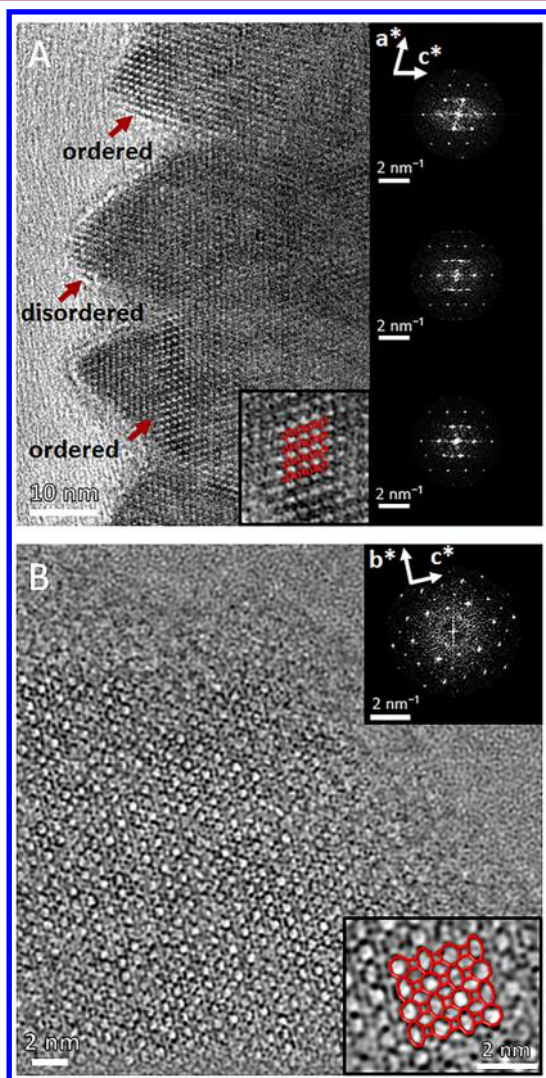


Figure 5. (A) Structure projections along the b -axis, reconstructed using the QFocus software from a through-focus series of 12 HRTEM images showing both ordered regions (top and bottom in A) and region containing disorders (middle in A), as indicated by the inserted Fourier transforms. (B) Structure projection along the a -axis, showing the ordered structure in the projection.

The three Fourier transforms also indicate that the crystal system is monoclinic rather than orthorhombic, so IM-18 may consist of intergrown monoclinic crystals. The reconstructed structure projection along the a -axis in Figure 5B shows that IM-18 is ordered in this projection.

Structure Refinement of As-Made IM-18. The major peaks in the PXRD pattern could be indexed using the program TOPAS⁴³ with an orthorhombic body-centered unit cell ($Imma$; $a = 5.255$ Å, $b = 14.952$ Å, $c = 16.981$ Å), equivalent to the one found using the RED data. However, refinement of the average structural model using the coordinates found from the RED data did not converge. Some weak reflections in the diffraction pattern could not be indexed. Initially, before we had

access to high quality HRTEM images and SAED patterns, three models were generated from the orthorhombic average structure with different arrangements of the $d4r$ units: a monoclinic one ($P2_1/m$; $a = 10.336$ Å, $b = 14.984$ Å, $c = 17.734$ Å, $\beta = 106.94^\circ$), and two orthorhombic ones ($Pmna$; $a = 14.984$ Å, $b = 10.336$ Å, $c = 16.965$ Å and $Pnmm$; $a = 16.965$ Å, $b = 10.336$ Å, $c = 14.984$ Å). Several possibilities were tried (see Supporting Information), but in the end we proceeded to refine the structure in the space group $P2_1/m$ because it was the only model that fitted all the data. The new HRTEM images, and in particular the Fourier Transform (FT) of these images, confirmed the monoclinic symmetry.

Rietveld refinement was initiated in the space group $P2_1/m$ using the program TOPAS.⁴⁴ The background was subtracted manually and improved during the course of the refinement. An anisotropic peak broadening model as described by Stephens⁴⁵ was introduced in order to better model the peak profiles. Geometric restraints were applied to all unique bond distances and angles, and the framework was optimized by refining the geometry. The initial scale factor was estimated by refining it for a few cycles using only the high-angle PXRD data (20–40°). As expected, in the subsequent difference electron density map (using all data), eight peaks were apparent in each channel along the b -axis (Figure S6). These arise from the $d4rs$ of the second framework and confirm the disorder in the structure. The second framework, shifted by $1/2a$ from the parent model, was introduced into the model. To improve the stability of the refinement, all x -coordinates of the second framework were constrained to those of the parent model (i.e., $x' = x + 0.5$).

A model of the OSDA was then generated and added to the model as a rigid body. The initial position of the OSDA in the 10-ring channels was estimated from the difference electron density map. In the space group $P2_1/m$ there are four OSDAs in the asymmetric unit (two in the parent framework and two in the second superimposed framework). Because they occupy essentially equivalent positions, the relative coordinates of all four OSDAs were constrained to be the same to maintain the stability of the refinement. Because the OSDA was found to lie with the pyridine ring perpendicular to the mirror plane, three carbon atoms (two from the pyridine ring and one methyl group) are symmetry equivalent, so the number of parameters to be refined could be reduced even further.

Next, bond and angle restraints for the OSDA, along with antibump restraints between the framework O atoms and the C and N atoms of the OSDA, were introduced. Our intention was to keep the pyridine ring and methyl groups flat and at reasonable distances from the framework. We gradually decreased the weights on the OSDA restraints, antibump restraints, and the flatten algorithm. Refinement was performed in very small steps to ensure that the geometry of the OSDA and the distances between the framework and the OSDA remained acceptable.

After the atomic positions of the OSDA had converged in the refinement, the Si/Ge ratio was refined and it converged to 3.2(1). This agrees well with the average ratio of 3.14 found using EDS (Table S2). The Ge atoms in IM-18 are located exclusively in $d4rs$. A difference electron density map revealed some electron density inside the $d4r$, and that was modeled as fluoride. The occupancy of the OSDA converged to 0.370(3) (0.5 for full occupancy). At this point, some residual electron density close to the methyl groups of the OSDA was observed. We thought that the OSDA might also be disordered, but attempts to include this in the model did not improve the

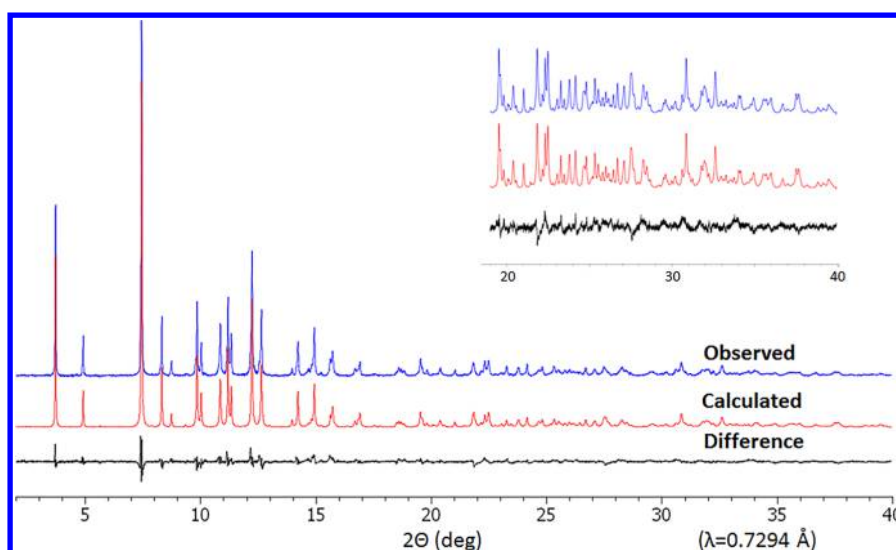


Figure 6. Observed (blue), calculated (red), and difference (black) profiles for the Rietveld refinement of IM-18 (sample 4).

refinement. This density probably arises from the fact that the DMAP is highly constrained and that its position overlaps with the $d4r$ of the second framework and/or from the presence of both protonated and nonprotonated DMAP. The remaining residual electron density is essentially featureless. The refinement finally converged with the agreement values $R_1 = 0.095$ and $R_{wp} = 0.117$ (Figure 6, Table 2). Most of the differences between the observed and calculated patterns can be attributed to the imperfect description of the peak shape.

Table 2. Crystallographic Data for As-Made IM-18 (Sample 4)

chemical composition (refined)	$I(C_7N_2H_{10})_{2.96}F_{2.37}[Si_{36.57}Ge_{11.43}O_{96}]$
space group	$P2_1/m$
a , Å	10.5089(5)
b , Å	14.9425(5)
c , Å	17.7775(7)
β , deg	107.323(4)
V , Å ³	2664.956(4)
2θ range, deg	2.000–39.984
λ , Å	0.7294
R_p	0.210
R_{wp}	0.117
R_1	0.095
observations	9477
reflections	2482
parameters	159
geometric restraints	148 (framework) and 12 (OSDA)

DISCUSSION

Description of the Structure of IM-18. The structure of IM-18 can be described in two ways. It can be viewed as a set of zigzag chains running in parallel to the a -axis connected via $d4r$ units to create two types of 8-ring channels parallel to the a -axis (Figure 7A). Zigzag chains are common in zeolite structures where one of the unit cell dimensions is around $n \times 5.2$ Å ($n = 1, 2, 3$, etc.).^{2,46} Alternatively, it can be viewed as a set of pillars of $d4r$ and mtw units running parallel to the b -axis (Figure 7B). The pillars are connected via shared edges to form layers parallel to the bc -plane. A $[4^25^48^2]$ unit with 8-ring openings,

which is also found in the UOS framework, is formed when the pillars are linked. These layers are then connected to one another to form 10-ring channels running parallel to the b -axis and 8-ring channels parallel to the c -axis.

The idealized framework structure of IM-18 has a 3D channel system, with straight 10-ring channels running parallel to the b -axis intersecting with 8-ring channels running parallel to the a - and c -axes (Figure S4). The 8-ring channels along a have an effective size of 2.62×3.38 Å and 6.04×1.83 Å (assuming an oxygen van der Waals radius of 1.35 Å) (Figure S4A). The channel along c is defined by two types of 8-ring openings that are alternating and slightly tilted with respect to the c -axis (Figure S4C) and have an effective size of 3.96×2.86 Å. There are two symmetry-independent straight 10-ring channels along b (Figure S4B), with effective sizes of 6.35×3.96 Å and 6.11×3.80 Å. These channels are eventually blocked by $d4rs$ because of the stacking disorder (i.e., a layer being shifted by $a/2$) (Figure S5). The idealized framework structure is present in the material in domains of 10 to 20 unit cells, but the real material has effectively only small pore openings. The 8-ring channels along the a - and c -axes allow only small molecules to enter, and the short 10-ring channels are blocked by the stacking disorder.

The structure refinement of IM-18 revealed that the OSDA molecules are sitting tightly between the $d4r$ units (Figure 7C). The refined occupancy of the OSDA is 0.370(3), which is lower than the expected value of 0.5, but not unusual. Similar partial occupancies for the OSDA were observed in the germanosilicate CIT-13⁴⁷ and the borosilicates SSZ-55 and SSZ-59.⁴⁸ The closest distances between the OSDA and the framework are 3.096 Å (C...O) and 3.227 Å (N...O). This is shown in the Hirshfeld surface⁴⁹ in Figure S7, where the contact points of the OSDA to the framework are visualized. We can observe that the OSDA molecules are slightly bent at the amino N atom. From the refined chemical formula $I(C_7N_2H_{10})_{2.96}F_{2.37}[Si_{36.57}Ge_{11.43}O_{96}]$ in Table 2, it is clear that not all of the DMAP molecules are protonated. There are not enough fluoride ions to balance the charge. Accordingly, the chemical formula for our IM-18 sample should be rewritten as $(I(C_7N_2H_{11})_{2.37}(C_7N_2H_{10})_{0.59}F_{2.37}[Si_{36.57}Ge_{11.43}O_{96}])$. This is consistent with the neutral-basic pH value in the (Si,Ge)-system, where the DMAP molecules are only partially

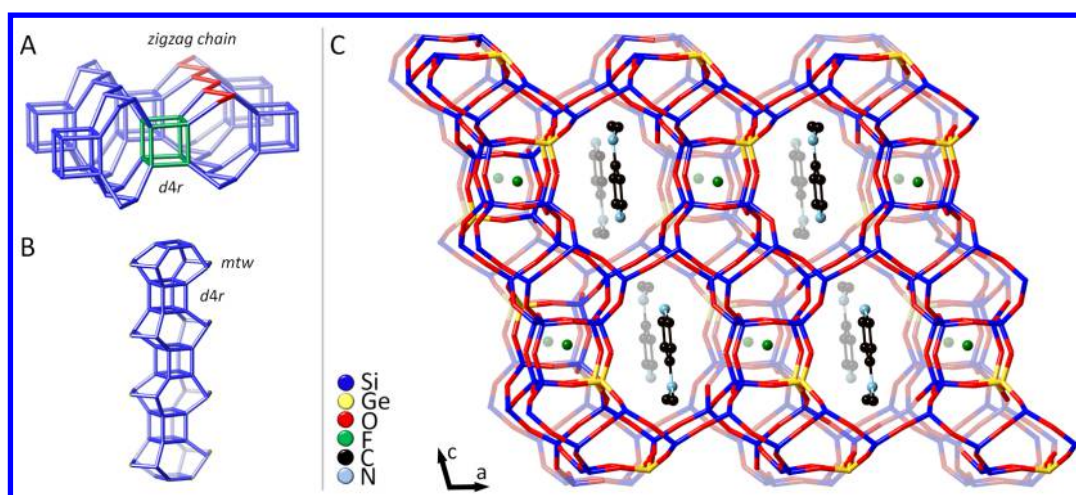


Figure 7. (A,B) Building units in IM-18. (C) Projection of IM-18 along the b -axis showing the position of the OSDA, germanium, and fluoride in the refined structure. T-sites with Ge occupancy of more than 50% are highlighted in yellow.

protonated. The methyl groups in the neutral and protonated DMAP will have slightly different locations, which could explain the residual density observed in the difference Fourier map. Contrary to expectations, no π -stacking of the protonated DMAP molecules that was observed inside the 12-ring channels of SSZ-51²⁹ is present in the case of IM-18. It is worth noting that the 4-dimethylaminopyridinium cation has been shown to adopt different packing arrangements in different 4-dimethylaminopyridinium salts.⁵⁰

The fluoride ions are located inside the $d4r$ s, slightly off center, perhaps because the Si/Ge distribution within the $d4r$ s is not symmetric (Figure 7). The refinement shows that only the T3 and T8 positions in the $d4r$ s contain a significant amount of Ge (0.38(1) and 0.28(2), respectively, where the maximum occupancy is 0.5). The average Si/Ge ratio in the $d4r$ s is 1.8. The final distances and angles are presented in Table 3.

Table 3. Framework Bond Angles and Distances after Rietveld Refinement of As-Made IM-18

	restraint	min	max	average
T–O–T (deg)	145.0	135.7	171.5	147.7
O–T–O (deg)	109.5	107.7	111.2	109.5
T–O (Å)	1.61	1.593	1.638	1.613

Disorder in IM-18. The structure of IM-18 can be built exclusively from single zigzag chains that are interconnected via $d4r$ units (Figure 7A). The structure refinement shows that the $d4r$ units connecting the zigzag chains can adopt two positions that are related by a translation of $1/2a$, and this results in a disordered framework. The arrangement of the $d4r$ units can be described as an ABCD-type stacking with c^* as the stacking direction. We can describe four independent stacking types: (1) ABCD, which can be considered the default stacking arrangement of IM-18 (Figure 8A); (2) ADCB, which is equivalent to (1), but mirrored across the ab -plane (Figure 8B); (3) a combination of domains of ABCD and ADCB stacked along the b -axis (Figure 8C); and (4) a combination of domains of ADCB and CBAD stacked along the b -axis (Figure 8D).

According to the diffuse streaks observed in the $[010]$ and $[001]$ zone-axis diffraction patterns (Figure 4B,C), which

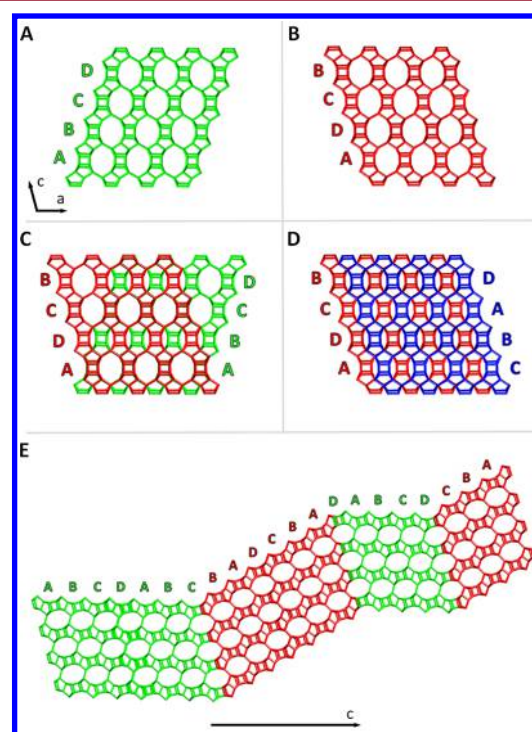


Figure 8. (A–D) Four main stacking arrangements along c^* that can appear in the structure of IM-18: (A) ABCD-type stacking, (B) ADCB-type stacking, (C) ABCD-ADCB stacked along the b -axis, and (D) ADCB-CBAD stacked along the b -axis. (E) Disorder model of IM-18 viewed along $[010]$ showing the interfaces between domains.

represent sections through diffuse planes, we can conclude that IM-18 has 1D long-range order and 2D disorder. This agrees with the disorder models described above. In a few crystals we did observe small satellite reflections and diffuse scattering (Figure S9) in the $[100]$ SAED patterns that would be indicative of 3D disorder, but we were not able to find a model that fits this observation.

To analyze the stacking sequences in the HRTEM images, we applied Fourier filtering on the image shown in Figure 5A using the diffraction spots and the diffuse streaks. In this way, noise can be removed and better contrast for long-range features obtained. This revealed domains of ABCD (green),

ADCB (red), and overlapping domains of the two (purple) as shown in Figure 9A. Stacking of ABCD (green) and ADCB

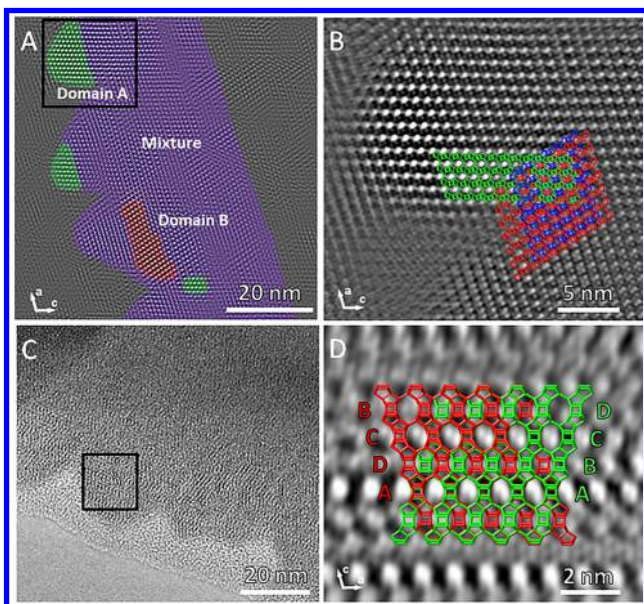


Figure 9. Possible stackings in IM-18 viewed along the b -axis that result in structure disorder. (A) Fourier filtered image of Figure 5A by using sharp diffraction spots and the diffuse streaks on the FFT that shows various domains; domain A in green, domain B in red, and overlapping domains in purple. (B) Enlarged area from (A) (marked by the square) showing how different domains of IM-18 can overlap. (C) Structure projection along the b -axis showing the disordered region. (D) Enlarged area from (C) showing possible stacking faults in IM-18.

(red) layers along the b -axis is better seen in Figure 9D, where the contrast in a small region in the HRTEM can be explained by the model in Figure 8C, with unblocked 10-ring channels shown as white contrast. Stacking faults of the nature ABCDCBA (Figure 8E), which describe the interface between ABCD- and ADCB-type domains, have also been found in HRTEM images (Figure 10). However, this situation was

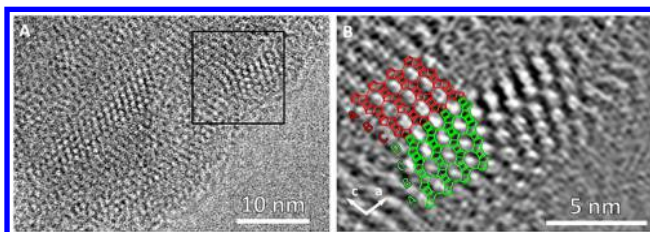


Figure 10. Stacking fault in IM-18 along the b -axis. (B) Fourier filtering of image (A) showing a small area with the stacking fault and the interface between the two domains. Two different stacking arrangements are shown in green (ABCD) and red (DCBA).

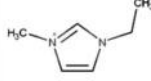
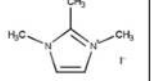
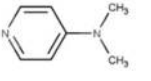
observed only rarely, and the image quality was limited by the beam damage of the material. Most images show a disorder that fits one of the four types described above. Rietveld refinement shows that the two domains (ABCD and ADCB) occur with equal probability, but we cannot say how often the stacking faults occur in the crystals.

The disorder found in IM-18 is fairly similar to that in the germanosilicate CIT-13,⁴⁷ for which the disorder was modeled through the PXRD. Although the structures are different, both

can be described in terms of a fixed silica-rich layer, and disordered $d4r$ units are related by the translation of $1/2a$ for IM-18 and $1/2c$ for CIT-13. In both cases, the PXRD data are free of line broadening, and therefore, we can say that these materials consist of at least medium-sized coherent domains (around 20–30 unit cells). The definitive answer about the disorder could not be given for CIT-13 due to the lack of HRTEM images. Our interpretation of the disorder in IM-18 is supported by the HRTEM images, which provide local information about the structure. Consequently, it can be said that the refined structure of IM-18 is in good agreement with the HRTEM images.

Comparison with ITQ-12 and IM-16. The structure of IM-18 is closely related to ITQ-12⁵¹ (ITW) and IM-16⁵² (UOS), but in different ways, as shown in Table 4 and Figure

Table 4. Comparison of IM-18, IM-16, and ITQ-12

	IM-16 (UOS)	ITQ-12 (ITW)	IM-18
Space group, Cell parameters	$Pm\bar{m}a$ $a = 19.91 \text{ \AA}$ $b = 7.55 \text{ \AA}$ $c = 9.07 \text{ \AA}$	$C2/m$ $a = 10.4 \text{ \AA}$ $b = 15.0 \text{ \AA}$ $c = 9.0 \text{ \AA}$ $\beta = 105.6^\circ$	$P2_1/m$ $a = 10.5 \text{ \AA}$ $b = 14.9 \text{ \AA}$ $c = 17.8 \text{ \AA}$ $\beta = 107.3^\circ$
No. of unique T-atoms	12 (Si/Ge)	12 (Si)	12 (Si/Ge)
Si/Ge ratio	4.5	not applicable	3
Chain	not applicable	Zigzag chain $\parallel a$ (two/unit cell)	Zigzag chain $\parallel a$ (five/unit cell)
Composite building units	$d4r, mtw$	$d4r$	$d4r, mtw$
Channel system	3D	2D	3D
Channel size	8-ring $\parallel b, c$ 10-ring $\parallel a$	8-ring $\parallel a, c$	8-ring $\parallel a, c$ 10-ring $\parallel b$
OSDA			

11. Like IM-18, ITQ-12 is also built from $d4r$ units and single zigzag chains (Figure 11A). In the idealized structure of IM-18, the $d4r$ units are at the same height in each layer, while in ITQ-12, alternate rows of $d4r$ units are shifted by $1/2a$. Both structures have similar projections along the a -axis, but the 8-ring channels are twisted in IM-18, while they are perpendicular to the channel in ITQ-12. This results in the different space groups for the two structures (Table 4). The relationship between IM-18 and ITQ-12 (ITW) can also be examined in terms of the orientations of the TO_4 tetrahedra in the $d4rs$ viewed along the a -axis (Figure 11A). While the TO_4 tetrahedra in the same layer are all pointing in the same direction (upward) in IM-18, only half of them are in ITQ-12.

IM-18 is also closely related to IM-16 (Figure 11B). The arrangement of building units ($d4r$ and mtw) within the layer is identical in the two frameworks. They differ in how the adjacent layers are related and stacked. In IM-16 the layers are related by a mirror plane perpendicular to the a -axis, while in IM-18 the layers are related by an inversion center. For IM-18, the $d4r$ – mtw pillar is also somewhat twisted as a result of the monoclinic symmetry. A similar situation can be found in ZSM-

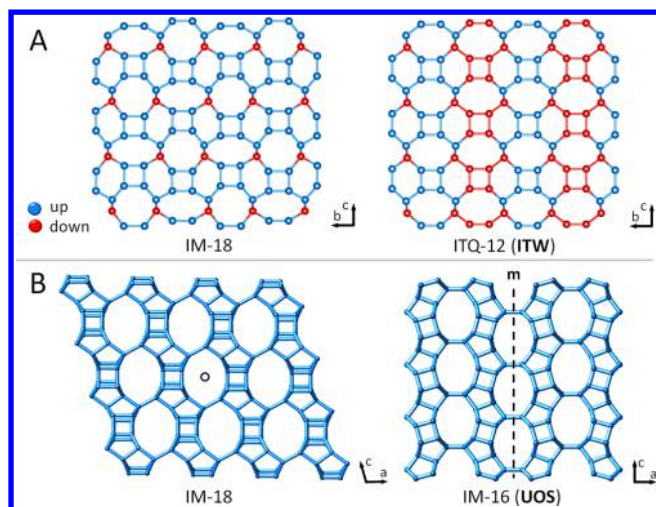


Figure 11. Comparison between IM-18 and ITQ-12 or IM-16. (A) Projections of IM-18 and ITQ-12 along the a -axis showing the orientations of the TO_4 tetrahedra. (B) Projections of IM-18 and IM-16 along the b -axis.

5 (MFI) and ZSM-11 (MEL).⁵³ These two framework topologies are built from the same layer, but successive layers are related by a mirror plane in MEL and by an inversion center in MFI.

Other Characterization Results. The TGA-DTA analysis (Figure S10) is consistent with the structure analysis. From the refined chemical formula $[(\text{C}_7\text{N}_2\text{H}_{10})_{2.96}\text{F}_{2.37}][\text{Si}_{36.57}\text{Ge}_{11.43}\text{O}_{96}]$, a weight loss of about 11.5% is expected for the DMAP and 1.2% for the fluoride species. On the TGA-DTA curve, an exothermic weight loss of 11.4% occurs between 250 and 750 °C that corresponds to the combustion of occluded DMAP molecules. Between room temperature and 250 °C, a two-step endothermic weight loss of 7.4% is attributed to the desorption of an excess of physisorbed water and DMAP on the surface of the crystals. The *in situ* PXRD study (Figure S11) showed that IM-18 is thermally stable even after a long period of exposure to humid atmosphere. The pore volume of calcined IM-18, as measured by nitrogen adsorption at 77 K, is 0.11 cm^3/g (Figure S12), which is half of that measured for IM-17, a large-pore UOV-type germanosilicate.⁵⁴ Thus, IM-18 is well described as a small-to-medium pore zeolite in accordance with the structure determination.

CONCLUSIONS

A new thermally stable microporous germanosilicate named IM-18 has been synthesized in fluoride medium using 4-methylaminopyridine as the OSDA. Its average crystal structure was solved from RED data, and then the details of the structure were derived by applying a combination of HRTEM and synchrotron PXRD techniques. IM-18 has a 3D channel system consisting of intersecting 10- and 8-ring channels but is multidimensionally disordered with stacking faults along both the b^* and c^* directions. Initial Rietveld refinement showed that there are two domains related by a shift of $1/2a$, and this proved to be key to the understanding of the disorder. Local information could then be gleaned from reconstructed structure projections of a through-focus series of HRTEM images. Further refinement revealed the location of the OSDA within the channels and the location of Ge in the $d4r$ units.

ASSOCIATED CONTENT

Supporting Information

The Supporting Information is available free of charge on the ACS Publications website at DOI: 10.1021/acs.cgd.8b00078.

Reconstructed 3D reciprocal lattice of IM-18 (AVI)

Tables S1–2, Figures S1–S12 (PDF)

Accession Codes

CCDC 1817538–1817539 contain the supplementary crystallographic data for this paper. These data can be obtained free of charge via www.ccdc.cam.ac.uk/data_request/cif, or by emailing data_request@ccdc.cam.ac.uk, or by contacting The Cambridge Crystallographic Data Centre, 12 Union Road, Cambridge CB2 1EZ, UK; fax: +44 1223 336033.

AUTHOR INFORMATION

Corresponding Authors

*E-mail: xzou@mmk.su.se.

*E-mail: jean-louis.paillaud@uha.fr.

ORCID

Magdalena O. Cichocka: 0000-0002-7829-1974

Stef Smeets: 0000-0002-5413-9038

Xiaodong Zou: 0000-0001-6748-6656

Present Address

[#]Laboratoire des Matériaux Céramiques et Procédés Associés (LMCPA), Université de Valenciennes et du Hainaut-Cambrésis, Pôle Universitaire de Maubeuge, Boulevard Charles de Gaulle, F-59600 Maubeuge, France.

Notes

The authors declare no competing financial interest.

ACKNOWLEDGMENTS

We thank the French National Centre for Scientific Research and IFP Energies nouvelles for a Doctoral grant to Y. L. (Agreement No. 50163400). We also thank the Swedish Governmental Agency for Innovation Systems (VINNOVA), the Swedish Research Council (VR), and the Knut and Alice Wallenberg Foundation (KAW) through the project grant 3DEM-NATUR. The authors acknowledge SOLEIL for allowance of synchrotron radiation facilities (proposal 20080373). S. S. thanks the Swiss National Science Foundation for financial support (project number: 165282). We thank Thomas Weber for valuable comments about the diffuse scattering.

REFERENCES

- (1) Li, H.; Yaghi, O. M. Transformation of Germanium Dioxide to Microporous Germanate 4-Connected Nets. *J. Am. Chem. Soc.* **1998**, *120*, 10569–10570.
- (2) Baerlocher, C.; McCusker, L. B. Database of Zeolite Structures. <http://www.iza-structure.org/databases/> (accessed Jul 14, 2017).
- (3) Conradsson, T.; Dadachov, M. S.; Zou, X. D. Synthesis and structure of $(\text{Me}_3\text{N})_6[\text{Ge}_{32}\text{O}_{64}] \cdot (\text{H}_2\text{O})_{4.5}$, a thermally stable novel zeotype with 3D interconnected 12-ring channels. *Microporous Mesoporous Mater.* **2000**, *41*, 183–191.
- (4) Li, J.; Corma, A.; Yu, J. Synthesis of new zeolite structures. *Chem. Soc. Rev.* **2015**, *44*, 7112–7127.
- (5) Paillaud, J.-L.; Caillet, P.; Brendlé, J.; Simon-Masseron, A.; Patarin, J. In *Functionalized Inorganic Fluorides: Synthesis, Characterization and Properties of Nanostructured Solids*; Tressaud, A., Ed.; John Wiley & Sons, 2010.
- (6) Zwijnenburg, M. A.; Bromley, S. T.; Jansen, J. C.; Maschmeyer, T. *Microporous Mesoporous Mater.* **2004**, *73*, 171–174.

- (7) Kamakoti, P.; Barckholtz, T. A. Computational insights into the role of Ge in stabilising double-four ring containing zeolites. *J. Phys. Chem. C* **2007**, *111*, 3575–3583.
- (8) Corma, A.; Rey, F.; Valencia, S.; Jordá, J. L.; Rius, J. A zeolite with interconnected 8-, 10- and 12-ring pores and its unique catalytic selectivity. *Nat. Mater.* **2003**, *2*, 493–497.
- (9) Paillaud, J.-L.; Harbuzaru, B.; Patarin, J.; Bats, N. Extra-Large-Pore Zeolites with Two-Dimensional Channels Formed by 14 and 12 Rings. *Science* **2004**, *304*, 990–992.
- (10) Corma, A.; Díaz-Cabañas, M. J.; Jordá, J. L.; Martínez, C.; Moliner, M. High-throughput synthesis and catalytic properties of a molecular sieve with 18- and 10-member rings. *Nature* **2006**, *443*, 842–845.
- (11) Sun, J.; Bonneau, C.; Cantín, Á.; Corma, A.; Díaz-Cabañas, M. J.; Moliner, M.; Zhang, D.; Li, M.; Zou, X. The ITQ-37 mesoporous chiral zeolite. *Nature* **2009**, *458*, 1154–1157.
- (12) Jiang, J.; Jorda, J. L.; Yu, J.; Baumes, L. A.; Mugnaioli, E.; Diaz-Cabanas, M. J.; Kolb, U.; Corma, A. Synthesis and Structure Determination of the Hierarchical Meso-Microporous Zeolite ITQ-43. *Science* **2011**, *333*, 1131–1134.
- (13) Luo, Y.; Smeets, S.; Peng, F.; Etman, A. S.; Wang, Z.; Sun, J.; Yang, W. Synthesis and Structure Determination of Large-Pore Zeolite SCM-14. *Chem. - Eur. J.* **2017**, *23*, 16829–16834.
- (14) Tang, L.; Shi, L.; Bonneau, C.; Sun, J.; Yue, H.; Ojuva, A.; Lee, B.-L.; Kritikos, M.; Bell, R. G.; Bacsik, Z.; Mink, J.; Zou, X. A zeolite family with chiral and achiral structures built from the same building layer. *Nat. Mater.* **2008**, *7*, 381–385.
- (15) Yun, Y.; Zou, X.; Hovmöller, S.; Wan, W. Three-dimensional electron diffraction as a complementary technique to powder X-ray diffraction for phase identification and structure solution of powders. *IUCrJ* **2015**, *2*, 267–282.
- (16) Smeets, S.; Berkson, Z. J.; Xie, D.; Zones, S. I.; Wan, W.; Zou, X.; Hsieh, M.-F.; Chmelka, B. F.; McCusker, L. B.; Baerlocher, C. Well-Defined Silanols in the Structure of the Calcined High-Silica Zeolite SSZ-70: New Understanding of a Successful Catalytic Material. *J. Am. Chem. Soc.* **2017**, *139*, 16803–16812.
- (17) Newsam, J. M.; Treacy, M. M. J.; Koetsier, W. T.; de Gruyter, C. B. Structural characterization of zeolite beta. *Proc. R. Soc. London, Ser. A* **1988**, *420*, 375–405.
- (18) Higgins, J. B.; LaPierre, R. B.; Schlenker, J. L.; Rohrman, A. C.; Wood, J. D.; Kerr, G. T.; Rohrbaugh, W. J. The framework topology of zeolite beta. *Zeolites* **1988**, *8*, 446–452.
- (19) Lobo, R. F.; van Koningsveld, H. New Description of the Disorder in Zeolite ZSM-48. *J. Am. Chem. Soc.* **2002**, *124*, 13222–13230.
- (20) Campbell, B. J.; Welberry, T. R.; Broach, R. W.; Hong, H.; Cheetham, A. K. Elucidation of zeolite microstructure by synchrotron X-ray diffuse scattering. *J. Appl. Crystallogr.* **2004**, *37*, 187–192.
- (21) Baerlocher, C.; Weber, T.; McCusker, L. B.; Palatinus, L.; Zones, S. I. Unraveling the Perplexing Structure of the Zeolite SSZ-57. *Science* **2011**, *333*, 1134–1137.
- (22) Zones, S. I.; Ruan, J.; Elomari, S.; Terasaki, O.; Chen, C. Y.; Corma, A. Studies on zeolite SSZ-57: a structural enigma. *Solid State Sci.* **2011**, *13*, 706–713.
- (23) Willhammar, T.; Sun, J.; Wan, W.; Oleynikov, P.; Zhang, D.; Zou, X.; Moliner, M.; Gonzalez, J.; Martínez, C.; Rey, F.; Corma, A. Structure and catalytic properties of the most complex intergrown zeolite ITQ-39 determined by electron crystallography. *Nat. Chem.* **2012**, *4*, 188–194.
- (24) Xie, D.; McCusker, L. B.; Baerlocher, C.; Zones, S. I.; Wan, W.; Zou, X. SSZ-52, a Zeolite with an 18-Layer Aluminosilicate Framework Structure Related to That of the DeNO_x Catalyst Cu-SSZ-13. *J. Am. Chem. Soc.* **2013**, *135* (28), 10519–10524.
- (25) Treacy, M. M. J.; Newsam, J. M.; Deem, M. W. A general recursion method for calculating diffracted intensities from crystals containing planar faults. *Proc. R. Soc. London, Ser. A* **1991**, *433*, 499–520.
- (26) Wan, W.; Sun, J.; Su, J.; Hovmöller, S.; Zou, X. Three-dimensional rotation electron diffraction: software RED for automated data collection and data processing. *J. Appl. Crystallogr.* **2013**, *46*, 1863–1873.
- (27) Butler, B. D.; Haefner, D. R.; Lee, P. L.; Welberry, T. R. High-energy X-ray diffuse scattering using Weissenberg flat-cone geometry. *J. Appl. Crystallogr.* **2000**, *33*, 1046–1050.
- (28) Lorgouilloux, Y.; Paillaud, J.-L.; Caultet, P.; Patarin, J.; Bats, N. French patent 2 923 477, November 11, 2007.
- (29) Morris, R. E.; Burton, A.; Bull, L. M.; Zones, S. I. SSZ-51-A New Aluminophosphate Zeotype: Synthesis, Crystal Structure, NMR, and Dehydration Properties. *Chem. Mater.* **2004**, *16*, 2844–2851.
- (30) Wan, W.; Hovmöller, S.; Zou, X. Structure projection reconstruction from through-focus series of high-resolution transmission electron microscopy images. *Ultramicroscopy* **2012**, *115*, 50–60.
- (31) Rietveld, H. M. A profile refinement method for nuclear and magnetic structures. *J. Appl. Crystallogr.* **1969**, *2*, 65–71.
- (32) Coati, A.; Chavas, L. M. G.; Fontaine, P.; Foss, N.; Guimaraes, B.; Gourhant, P.; Legrand, P.; Itie, J.-P.; Fertey, P.; Shepard, W.; Isabet, T.; Sirigu, S.; Solari, P.-L.; Thiaudiere, D.; Thompson, A. Status of the crystallography beamlines at synchrotron SOLEIL. *Eur. Phys. J. Plus* **2017**, *132*, 174.
- (33) Itie, J.-P.; Baudalet, F.; Briois, V.; Elkaim, E.; Nadji, A.; Thiaudière, D. In *X-Rays and Materials*; Goudeau, P., Guinebretière, R., Eds.; John Wiley & Sons, Inc., 2012; pp 1–47.
- (34) de Boer, J. H.; Lippens, B. C.; Linsen, B. G.; Broekhoff, J. C. P.; van den Heuvel, A.; Osinga, T. J. The θ -curve of multimolecular N₂-adsorption. *J. Colloid Interface Sci.* **1966**, *21*, 405–414.
- (35) Rollmann, L. D.; Valyocsik, E. W. US patent US4423021 A, December 27, 1983.
- (36) Hua, W.; Chen, H.; Yu, Z.-B.; Zou, X.; Lin, J.; Sun, J. A Germanosilicate Structure with 11 × 11 × 12-Ring Channels Solved by Electron Crystallography. *Angew. Chem., Int. Ed.* **2014**, *53*, S868–S871.
- (37) Blasco, T.; Corma, A.; Díaz-Cabañas, M. J.; Rey, F.; Vidal-Moya, J. A.; Zicovich-Wilson, C. M. Preferential Location of Ge in the Double Four-Membered Ring Units of ITQ-7 Zeolite. *J. Phys. Chem. B* **2002**, *106*, 2634–2642.
- (38) Sastre, G.; Vidal-Moya, J. A.; Blasco, T.; Rius, J.; Jordá, J. L.; Navarro, M. T.; Rey, F.; Corma, A. Preferential Location of Ge Atoms in Polymorph C of Beta Zeolite (ITQ-17) and Their Structure-Directing Effect: A Computational, XRD, and NMR Spectroscopic Study. *Angew. Chem., Int. Ed.* **2002**, *41*, 4722–4726.
- (39) Pulido, A.; Sastre, G.; Corma, A. Computational Study of 19F NMR Spectra of Double Four Ring-Containing Si/Ge-Zeolites. *ChemPhysChem* **2006**, *7*, 1092–1099.
- (40) Sheldrick, G. M. A short history of SHELX. *Acta Crystallogr., Sect. A: Found. Crystallogr.* **2008**, *64*, 112–122.
- (41) Baerlocher, C.; Hepp, A.; Meier, M. DLS-76, A Program for the Simulation of Crystal Structures by Geometric Refinement; Institute of Crystallography and Petrography, ETH Zurich: Zurich.
- (42) Kirkland, E. J.; Siegel, B. M.; Uyeda, N.; Fujiyoshi, Y. Digital reconstruction of bright field phase contrast images from high resolution electron micrographs. *Ultramicroscopy* **1980**, *5*, 479–503.
- (43) Coelho, A. A. Indexing of powder diffraction patterns by iterative use of singular value decomposition. *J. Appl. Crystallogr.* **2003**, *36*, 86–95.
- (44) Coelho, A. A. TOPAS-ACADEMIC, v4.1.
- (45) Stephens, P. W. Phenomenological model of anisotropic peak broadening in powder diffraction. *J. Appl. Crystallogr.* **1999**, *32*, 281–289.
- (46) Guo, P.; Yan, N.; Wang, L.; Zou, X. Database Mining of Zeolite Structures. *Cryst. Growth Des.* **2017**, *17*, 6821–6835.
- (47) Kang, J. H.; Xie, D.; Zones, S. I.; Smeets, S.; McCusker, L. B.; Davis, M. E. Synthesis and Characterization of CIT-13, a Germanosilicate Molecular Sieve with Extra-Large Pore Openings. *Chem. Mater.* **2016**, *28*, 6250–6259.
- (48) Smeets, S.; McCusker, L. B.; Baerlocher, C.; Elomari, S.; Xie, D.; Zones, S. I. Locating Organic Guests in Inorganic Host Materials from X-ray Powder Diffraction Data. *J. Am. Chem. Soc.* **2016**, *138*, 7099–7106.

(49) Spackman, M.; Jayatilaka, D. Hirshfeld surface analysis. *CrystEngComm* **2009**, *11*, 19–32.

(50) Mayr-Stein, R.; Bolte, M. 4-Dimethylaminopyridinium bromide. *Acta Crystallogr., Sect. C: Cryst. Struct. Commun.* **2000**, *56*, e19–e20.

(51) Yang, X.; Cambor, M. A.; Lee, Y.; Liu, H.; Olson, D. H. Synthesis and Crystal Structure of As-Synthesized and Calcined Pure Silica Zeolite ITQ-12. *J. Am. Chem. Soc.* **2004**, *126*, 10403–10409.

(52) Lorgouilloux, Y.; Dodin, M.; Paillaud, J.-L.; Caullet, P.; Michelin, L.; Josien, L.; Ersen, O.; Bats, N. IM-16: A new microporous germanosilicate with a novel framework topology containing *d4r* and *mtw* composite building units. *J. Solid State Chem.* **2009**, *182*, 622–629.

(53) Ohsuna, T.; Terasaki, O.; Nakagawa, Y.; Zones, S. I.; Hiraga, K. Electron Microscopic Study of Intergrowth of MFI and MEL: Crystal Faults in B-MEL. *J. Phys. Chem. B* **1997**, *101*, 9881–9885.

(54) Lorgouilloux, Y.; Dodin, M.; Mugnaioli, E.; Marichal, C.; Caullet, P.; Bats, N.; Kolb, U.; Paillaud, J.-L. IM-17: a new zeolitic material, synthesis and structure elucidation from electron diffraction ADT data and Rietveld analysis. *RSC Adv.* **2014**, *4*, 19440–19449.